

Energy and productivity efficient vacuum pressure swing adsorption process to separate CO₂ from CO₂/N₂ mixture using Mg-MOF-74: A CFD simulation

Naef A.A. Qasem*, Rached Ben-Mansour

Mechanical Engineering Department and KACST-TIC on CCS, King Fahd University of Petroleum & Minerals, Dhahran 31261, Saudi Arabia

HIGHLIGHTS

- VPSA for separating CO₂ from CO₂ + N₂ using Mg-MOF-74 is numerically investigated.
- Two- and three-dimensional models are presented using UDF-ANSYS Fluent program.
- Regeneration time is tuned to optimize the VPSA performance.
- The VPSA performance indices show a substantial improvement in the CO₂ separation.

ARTICLE INFO

Keywords:

Adsorption
Carbon capture
Carbon-dioxide
Separation
VPSA
CFD
Mg-MOF-74

ABSTRACT

Quantitatively, carbon dioxide is the main gas emitted from the burning of fossil fuels; thus, it is the primary contributor to global warming. However, climate change could be mitigated using “carbon capture and storage” (CCS) methods. CO₂ separation by physical adsorption is a promising technology to achieve CO₂ capture with minimum energy costs. Mg-MOF-74 is a distinguished adsorbent amongst porous materials owing to its high CO₂ uptake under flue gas conditions. In this study, a vacuum pressure swing adsorption (VPSA) process composed of five steps (pressurization, feed, rinse, blowdown, and purge) for separating CO₂ from a CO₂/N₂ mixture using Mg-MOF-74 was mathematically modeled. Two- and three-dimensional computational fluid dynamics (CFD) models were developed using a user-defined-function (UDF, written in C) linked to the ANSYS Fluent program. The models have been validated against published pressure swing adsorption experimental data. The regeneration (blowdown and purge) time has been tuned to explore the performance improvement for the VPSA process. The key optimum performance indices for VPSA in terms of CO₂ purity, recovery, productivity, and process power consumption were found to be 95.3%, 94.8%, 0.50 kg.CO₂ h^{−1} kg.MOF^{−1}, and 68.71 kW h tonne.CO₂^{−1}, respectively. The corresponding operating carbon capture cost has been evaluated as \$6.87 tonne.CO₂^{−1} for a 500-MW post-combustion power plant. These CO₂ productivity and power consumption performances represent a significant enhancement in CO₂ separation using physical adsorption technology compared to those reported in the literature.

1. Introduction

Climate change resulting from greenhouse gases is a global problem that threatens life on Earth. Greenhouse gases include carbon dioxide, water vapor, nitrogen oxide, and methane. Global warming is caused by these gases and has resulted in atmospheric heat waves, shore floods, droughts, destruction of cold water marine life, and whole ecosystems, as well as economic losses, which are expected to reach 5–20% of the world's gross domestic product [1]. The global temperature over the last 100 years has increased by about 0.74% and is expected to increase by 6.4% by the end of this century [1]. As a result, huge quantities of

sea and glacier ice have been melting, causing at least a 0.2-mm per year rise in global sea level [2]. The predominant greenhouse gas is carbon dioxide [3]. Globally, fossil fuels are the prevailing primary source of energy and will continue to be so for the next few decades. Because carbon dioxide (CO₂) is considered to be one of the main promoters of climate change, carbon capture (CC) is an essential solution to allow the continued use of fossil fuels while minimizing CO₂ emissions, thereby mitigating global climate change. Research is the only way to address the technical challenges of carbon capture such as improving the efficiency and reducing the cost of CO₂ capture [4].

The number of investigations related to carbon capture and storage

* Corresponding author.

E-mail address: naefqasem@kfupm.edu.sa (N.A.A. Qasem).

Nomenclature

C	Concentration, mol m^{-3}
C_p	Specific heat capacity, $\text{J kg}^{-1} \text{K}^{-1}$
D, d	Diameter, size, m
D_{disp}	Mass dispersion coefficient, $\text{m}^2 \text{s}^{-1}$
E_g	Total gas energy, J m^{-3}
E_s	Total adsorbent energy, J m^{-3}
h	Sensible enthalpy, J kg^{-1}
h_{ext}	External heat transfer coefficient, $\text{W m}^{-2} \text{K}^{-1}$
h_{int}	Internal heat transfer coefficient, $\text{W m}^2 \text{K}^{-1}$
ΔH	Heat of adsorption, J mol^{-1}
\vec{g}	Gravity acceleration vector, m s^{-2}
\vec{J}	Diffusion flux, $\text{kg m}^{-2} \text{s}^{-1}$
K_o	Toth adsorption constants, Pa^{-1}
K_{eq}	Isotherm adsorption constant, Pa^{-1}
k	Thermal conductivity, $\text{W m}^{-1} \text{K}^{-1}$
k_L	Linear driving force adsorption time constant, s^{-1}
M	Molecular weight, kg mol^{-1}
n	Isotherm adsorption constant
q	Adsorption uptake, mmol g^{-1}
q^*	Equilibrium adsorption uptake, mmol g^{-1}
q_m	Adsorption uptake limit, mmol g^{-1}
Q_F	Feed volumetric flow rate, $\text{m}^3 \text{s}^{-1}$
P	Pressure, Pa
R	Universal gas constant, $\text{J mol}^{-1} \text{K}^{-1}$
r	Radius, m
Re	Reynolds number

t	Time, s
T	Temperature, K
$\vec{\tau}$	Stress tensor, N m^{-2}
y	Mass fraction
\vec{v}	Velocity vector, m s^{-1}

Greek letters

ρ	Mixture gas density, kg m^{-3}
ε	Bed porosity
ϵ	Thermal emissivity
μ	Dynamic viscosity, Pa s^{-1}
σ	Stefan-Boltzmann coefficient, $\text{W m}^{-2} \text{K}^{-4}$

Subscript

eff	Effective
p	Particle
pore	Adsorbent pore
i	Gas species index
g	Gas
max	Maximum
min	Minimum
tot	Total
s	Standard conditions
0	Inlet, saturation
w	Wall

(CCS) is growing every day. Many researchers have studied CO_2 separation and storage using both experimental and simulation methods, as well as developing novel adsorbents for this purpose [5]. The most attractive reason for using adsorption for CO_2 separation is the ease of the regeneration of the adsorbent material, which is achieved by applying heat or a vacuum or both [6]. Activated carbons (AC) and zeolites are the most commonly used adsorbents for CO_2 separation and storage. Zeolites are more popular than activated carbon for CO_2 capture and hydrogen storage in low-pressure applications [7,8], whereas activated carbon materials are desirable for high-pressure processes [8,9]. However, the obvious merits of activated carbon materials over zeolites include cost-effectiveness, hydro-stability, and lower energy requirements for regeneration because of their lower heat of adsorption [10]. Recently, a novel class of porous materials has been synthesized, so-called metal-organic frameworks (MOFs) [11]. Currently, MOF-74 is the most available MOF, having a high CO_2 adsorption capacity and an excellent CO_2 over N_2 selectivity [12,13]. More specifically, Mg-MOF-74 has been quantitatively identified as the best CO_2 adsorbent at low-pressure conditions (350 mg g^{-1} at 298 K and 1 bar) [13].

A considerable number of experimental and numerical investigations based on CO_2 capture and separation have been conducted so far in terms of pressure and vacuum swing adsorption [14–20]. A column bed with two layers of different adsorbents (zeolite 13X and carbon molecular sieves 3K) has been investigated to separate $\text{CH}_4/\text{CO}_2/\text{N}_2$ using the pressure swing adsorption (PSA) method [14]. The produced gas had 88.8% and 66.2% methane purity and recovery, respectively, at 323 K , and the remaining percentages were mostly CO_2 . Carbon capture by vacuum swing adsorption (VSA) was conducted by Chaffee et al. [15]. Their results showed that the carbon dioxide purity, recovery, and power consumption were about 95%, 70%, and $6 \text{ kW (tonne CO}_2 \text{ Day}^{-1})^{-1}$, respectively, when carrying out nine steps of vacuum swing adsorption (VSA) using the 13X zeolite. A two-stage PSA process was used to separate CO_2 from a CO_2/N_2 (10.5%/89.5% molar-base) mixture and achieved 99%, 80%, and $0.28 \text{ kW h Nm}^3 \text{ CO}_2^{-1}$ CO_2 purity, recovery, and power consumption, respectively [16]. The optimal CO_2

purity and recovery were investigated by Choi et al. [17], and they obtained values of about 95% and 72%, respectively. Dantas et al. [18] also used 13X to separate CO_2 from a gas mixture composed of 15 vol% CO_2 and 85 vol% N_2 using the PSA method. The results showed the best CO_2 purity and recovery were about 36.8% and 90%, respectively. PSA has also been used to separate CO_2 from a gas mixture composed of 8.33% CO_2 , 33.3% N_2 , and 58.3% He [19]. The study showed that increasing the amount of inert gas (He) significantly improved the CO_2 recovery, although the CO_2 purity decreased sharply. Another VSA process used to separate CO_2 from a 15% CO_2 and 85% N_2 gas mixture showed that the CO_2 purity, recovery, productivity, and power consumption were about 95.9%, 86.4%, $1.4 \text{ tonne CO}_2 \text{ m}^{-3} \text{ day}^{-1}$, and $339 \text{ kW h tonne CO}_2^{-1}$, respectively [20]. Furthermore, some experimental and numerical investigations of CO_2 removal from flue gas using natural and synthetic zeolites have indicated that synthetic zeolites (such as 5A and 13X) are the most encouraging adsorbents for CO_2 capture from combustion products [21–24]. Zeolite 13X-APG was used for CO_2 separation using an experimental vacuum pressure swing adsorption (VPSA) technique by Wang et al. [25]. The results showed that CO_2 recovery and purity were about 85–95% and 37–82%, respectively, with a power consumption of about $1.79\text{--}2.14 \text{ MJ kg CO}_2^{-1}$ and a CO_2 productivity of about $0.207 \text{ mol CO}_2 \text{ m}^{-3}$ of adsorbent. Zeolite 13X-APG was also utilized [26] for post combustion CO_2 capture by a vacuum temperature swing adsorption (VTSA) process. The study concentrated mainly on the type of regeneration process, such as temperature swing adsorption (TSA), VSA, or VTSA, to find the best CO_2 recovery and purity. The three regeneration methods (TSA, VSA, and VTSA) were compared. The CO_2 recovery and purity when using the VSA process were 8.6% and 78.4%, respectively, at $P = 3 \text{ kPa}$ for 5 min of evacuation and 0.15 standard liter per minute (SLPM) of N_2 purging. The TSA process without evacuation achieved 78.1% of CO_2 recovery and 91.6% of CO_2 purity at a desorption temperature of 443 K . The cooling was carried out close to ambient conditions for 10 min to increase the adsorption uptake. Conversely, VTSA at 403 K and 3 kPa achieved 98.2% and 94% of CO_2 recovery and purity, respectively. A

novel electric swing adsorption process was proposed to regenerate polyethylenimine-impregnated carbon spheres [27]. Microwave swing regeneration could also be used for CO₂ chemical adsorption separation and reduced the energy consumption and amine degradation [28]. An adsorbent of amine-loaded carbon nanotubes was investigated for CO₂ separation by dual-column temperature/vacuum swing adsorption [29]. Elevated-temperature pressure swing adsorption was used to minimize the energy consumption for an integrated gasification combined cycle with carbon dioxide capture [30]. The utilization of AC for CO₂ swing adsorption separation was found to consume lower energy than zeolite although it adsorbed lower quantities of CO₂. For example, CO₂ productivity and energy consumption using AC were about 0.035 kg CO₂ h⁻¹ kg adsorbent⁻¹ and 723.6 kJ kg CO₂⁻¹ [31]. The regeneration of an AC (DARCO FGD, Norit) at > 373 K achieved 100% CO₂ purity and more than 50% recovery using the TSA process [32]. A green-coffee-based CO₂ adsorbent was used as adsorbent for CO₂ VTSA post combustion capture. The performance indices obtained from the process were 75% CO₂ purity and 84% CO₂ recovery with a productivity of 0.066 kg CO₂ h⁻¹ kg adsorbent⁻¹ [33]. In addition, the pre-hydration of a CaO-based pellet adsorbent improved CO₂ capture at ambient temperatures [34].

The energy consumed in chemical absorption/adsorption capture is more expensive than that in physical adsorption. For instance, a re-boiler heat duty value of 2.74 GJ tonne CO₂⁻¹ has been achieved in the amine-based post combustion capture process in a 650-MW power plant [35].

The cost of CO₂ capture was about \$60 tonne CO₂⁻¹ using amine-scrubbing (chemical absorption), while it was almost \$12 tonne CO₂⁻¹ when carrying out physical VSA using 13X in a 500-MW power plant [36]. The National Energy Technology Laboratory (NETL), USA, has proposed CO₂ capture from a fired-power plant using a phase-changing CO₂-capture adsorbent, aiming to obtain 95% CO₂ purity at the cost of \$40 tonne CO₂⁻¹ by 2025 and a cost of < \$10 tonne CO₂⁻¹ by 2035 [37].

Generally, investigations have focused on obtaining highly pure CO₂ with a high recovery level. However, acquiring high levels of both CO₂ purity and recovery (> 90% for each) from swing adsorption processes is still a challenge. The obtained CO₂ productivity is still below 0.1 kg CO₂ h⁻¹ kg adsorbent⁻¹ using conventional adsorbents (as carbon-based materials and zeolites). Moreover, the energy consumption of CO₂ separation is high (> 720 kJ kg CO₂⁻¹ [16,26,31]). In this scenario, the superior CO₂ adsorption capacity and selectivity of MOFs, especially Mg-MOF-74, under flue gas conditions make them promising candidates to replace conventional adsorbents (AC, zeolites, and silica gels) for CO₂ separation applications with a lower energy cost. However, most MOFs have only been characterized by CO₂ adsorption isotherms, which do not represent the CO₂ dynamic separation processes.

Concerning numerical investigations, published numerical swing adsorption processes are governed by 1D models [17,26,38], as developed by Silva et al. [39], to investigate cyclic adsorption processes (PSA/VSA and TSA). Therefore, multi-dimensional simulation modeling is required to increase the accuracy of swing adsorption modeling. The advantages of using 2D/3D adsorption models are the following. Including two or three dimensions improves the accuracy of the heat and mass transfer results because of the computation of thermal and mass diffusions in two or three directions. It is also easy to present the results using contours to highlight the actual distribution of parameters (such as molar fractions, temperature, adsorption quantities, and flow rates) along the adsorbent beds. Moreover, three-dimensional modeling can be applied to simulate adsorption processes in complex bed geometries. The disadvantage of using 2D/3D models is the longer time of running the required simulations in comparison to 1D models.

Considering the gaps in the literature and the crucial need to improve the performance indices (> 90% of CO₂ purity and recovery, > 0.2 kg CO₂ h⁻¹ kg adsorbent⁻¹ of CO₂ productivity, and < 500 kJ kg CO₂⁻¹ of power consumption, associated with a CO₂ separation

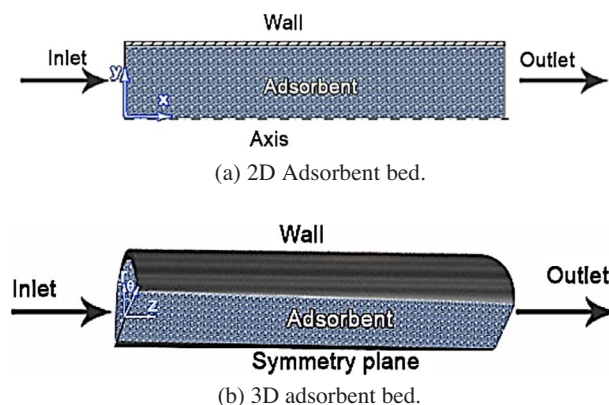


Fig. 1. Adsorbent beds used for CO₂ separation.

process costing less than \$10 tonne CO₂⁻¹), this work aims to introduce an alternative adsorption computational model to carry out an accurate 2D/3D vacuum pressure swing adsorption simulations. The developed model will be employed for separating CO₂ from a binary gas mixture composed of 15 vol% CO₂ and 85 vol% N₂ using Mg-MOF-74 to enhance the performance of CO₂ separation technology. We will highlight the advantages of utilizing Mg-MOF-74 for CO₂ separation and will explore the optimal VPSA performance by finding the optimum regeneration period. Therefore, the optimal performance will address the minimum carbon capture cost to be attractive for CO₂ capture in power plants and the industrial sector.

2. Numerical modeling methods

2.1. Adsorbent bed and model description

The used adsorbent bed was a cylinder filled with adsorbent material (13X or Mg-MOF-74), as shown in Fig. 1. Axisymmetric 2D (Fig. 1(a)) and symmetry 3D (Fig. 1(b)) beds have been considered for modeling in this study.

The simulation model is based on the momentum, mass, and energy conservation equations. The computational fluid dynamics (CFD) model was developed using a user define function (UDF, written in C) connected to the ANSYS Fluent program [40] to estimate the gas adsorption isotherms and kinetics and adjust the source terms of mass, momentum, and energy equations. The model is valid for multiple dimensions and various geometries.

For all studied cases, the following assumptions were adopted:

- the gas phase obeys ideal gas law,
- the flow is laminar,
- the porous medium is homogenous,
- the physical properties of the adsorbents are constant, and
- the linear driving force (LDF) model is used to account for the mass transfer rate during the adsorption process.

In addition, the isotherms were accurately fitted from the experimental isotherms according to the appropriate approaches such as Toth and dual-site Langmuir.

2.2. Mass conservation equations

The mass conservation equation calculates the local mass fraction of each species through the solution of the convection-diffusion equation of all species as:

$$\varepsilon \frac{\partial(\rho y_i)}{\partial t} + \nabla \cdot (\rho \vec{v} y_i) = -\nabla \cdot (-\varepsilon \rho D_{disp} \nabla y_i) - (1-\varepsilon) \rho_p M_i \frac{\partial q_i}{\partial t}, \quad (1)$$

where ρ (kg m⁻³) is the gas density, y_i is the mass fraction of species i

(CO₂ and N₂), \vec{v} (m s⁻¹) is the velocity vector, ε is the bed porosity, D_{disp} (m² s⁻¹) is the mass dispersion coefficient, M_i (kg mol⁻¹) is the molecular weight of species i , q_i (mmol g⁻¹) is the adsorbent amount of component i , and t (s) is the time.

The overall mass balance is

$$\varepsilon \frac{\partial(\rho)}{\partial t} + \nabla \cdot (\rho \vec{v}) = -(1-\varepsilon)\rho_p \sum_i M_i \frac{\partial q_i}{\partial t}. \quad (2)$$

2.3. Momentum conservation equation

The momentum equation of the gases flow can be expressed as:

$$\varepsilon \frac{\partial(\rho \vec{v})}{\partial t} + \nabla \cdot (\rho \vec{v} \vec{v}) = -\nabla P + \nabla \cdot \vec{\tau} + \rho \vec{g} + S, \quad (3)$$

where P (Pa) is the operating pressure, $\vec{\tau}$ (N m⁻²) is the stress tensor, \vec{g} (m s⁻²) is the gravity acceleration vector, and S (N m⁻³) is the momentum source term in the porous media. Its component in the i -direction can be calculated from the Ergun equation including inertia and viscous resistances as:

$$S_i = -\left(\frac{\mu}{\kappa} v_i + C_2 \frac{1}{2} \rho |\vec{v}| v_i\right), \quad (4)$$

where μ (Pa s) is the dynamic gas viscosity, $1/\kappa$ (m⁻²) is the porous media viscous resistance, C_2 (m⁻¹) is the inertial resistance, $|\vec{v}|$ is the value of the velocity vector, and v_i is the velocity component in the i -direction.

2.4. Energy conservation equation

The energy equation for CO₂ separation shows the balance between the energy stored in the adsorbent bed and the change in energy arising from convective flow, pressure work, thermal diffusion, and advection, as well as the energy released or consumed by the adsorption and desorption processes:

$$\begin{aligned} \frac{\partial}{\partial t} [\varepsilon \rho E_g + (1-\varepsilon)\rho_p E_s] + \nabla \cdot [\vec{v}(\rho E_g + P)] \\ = \nabla \cdot [k_{eff} \nabla T - \sum_i h_i \vec{J}_i + \vec{\tau} \cdot \vec{v}] + (1-\varepsilon)\rho_p \sum_i \Delta H_i \frac{\partial q_i}{\partial t}, \end{aligned} \quad (5)$$

where E_g (J m⁻³) is the total gas energy, E_s (J m⁻³) is the total adsorbent energy, ΔH (J mol⁻¹) is the heat of adsorption, which is different from one material to another and sometimes also varies with variation of gas adsorbed amounts, T (K) is the equilibrium temperature, h_i (J kg⁻¹) is the sensible enthalpy ($h = \sum_i y_i h_i$), and \vec{J}_i (kg m⁻² s⁻¹) is the diffusion flux of the gas component i .

The parameter k_{eff} is the effective conductivity of the adsorbent bed and can be expressed as:

$$k_{eff} = \varepsilon k_g + (1-\varepsilon)k_s, \quad (6)$$

where k_g and k_s (W m⁻¹ K⁻¹) are the thermal conductivities of the gas mixture and adsorbent, respectively.

For the wall metal, the energy equation through the walls depends upon the balance of heat stored in the wall and the heat diffusion through it as follows.

$$\frac{\partial}{\partial t} (\rho_w C_w T_w) = \nabla \cdot (k_w \nabla T_w), \quad (7)$$

where ρ_w (kg m⁻³) is the wall density, C_w (J kg⁻¹ K⁻¹) is the wall heat capacity, T_w (K) is the local temperature of the wall, and k_w (W m⁻¹ K⁻¹) is the thermal conductivity of the wall material.

2.5. Adsorption isotherm and kinetics models

The equilibrium adsorption isotherms are represented by different

models according to the accuracy of the fitting from the experimental isotherms. Toth and dual-site Langmuir models are used for the equilibrium adsorption of gases.

Toth model

$$q_i^* = \frac{q_{m,i} K_{eq,i} y_i P}{(1 + (K_{eq,i} y_i P)^{n_i})^{(1/n_i)}} \quad (8)$$

Here, $q_{m,i}$ (mmol g⁻¹) is the maximum adsorbed amount of species i , $K_{eq,i}$ (Pa⁻¹) is an adsorption constant that can be calculated as a function of temperature (Eq. (9)), and n_i is the adsorption constant.

$$K_{eq,i} = k_0 e^{-\left(\frac{\Delta H}{RT}\right)} \quad (9)$$

Here, k_0 (Pa⁻¹) is a temperature-independent constant.

Dual-site Langmuir model

$$q_i^* = \frac{q_{m,i1} K_{eq,i1} y_i P}{1 + K_{eq,i1} y_i P} + \frac{q_{m,i2} K_{eq,i2} y_i P}{1 + K_{eq,i2} y_i P} \quad (10)$$

Here, $q_{m,i1}$ and $q_{m,i2}$ (mmol g⁻¹) represent the maximum adsorbed amount of species i , and $K_{eq,i1}$ and $K_{eq,i2}$ (Pa⁻¹) are adsorption constants that depend on the adsorbent temperature.

The adsorption kinetics are evaluated by the LDF model as follows:

$$\frac{\partial q_i}{\partial t} = k_{L,i} (q_i^* - q_i). \quad (11)$$

The parameter q_i (mmol g⁻¹) represents the actual adsorbed amount, q_i^* (mmol g⁻¹) is the equilibrium adsorbed amounts, and $k_{L,i}$ (s⁻¹) is the adsorption time constant, which is approximately estimated from complex diffusion and concentrations of species. $k_{L,i}$ is expressed by the film transfer coefficient and macroporous and microporous resistances of the gases passing through the porous materials:

$$\frac{1}{k_{L,i}} = \frac{r_p q_{0,i}}{3k_{f,i} C_{0,i}} + \frac{r_p^2 q_{0,i}}{15\varepsilon_p D_{p,i} C_{0,i}} + \frac{r_c^2}{15D_{c,i}}, \quad (12)$$

where $q_{0,i}$ and $C_{0,i}$ (mol m⁻³) are the values of the concentrations in the solid and gas phases, respectively, r_p (m) is the adsorbent particle radius, ε_p is the particle porosity, and r_c is the adsorbent crystal radius. $k_{f,i}$, $D_{p,i}$, and $D_{c,i}$ are the film mass transfer coefficient, macroporous diffusion coefficient, and microporous diffusion coefficient, respectively, for component i . The evaluation of these coefficients has been explained previously [41,42]. Eq. (12) is mainly used for linear isothermal systems. However, it also works reasonably well for non-linear systems [43].

2.6. General boundary conditions

2.6.1. External walls

The heat transfer between the bed wall and the ambient can be expressed as:

$$k_w \left(\frac{\partial T_w}{\partial n} \right)_w = h_{ext} (T_w - T_{amb}) + \varepsilon \sigma (T_w^4 - T_{amb}^4), \quad (13)$$

where n (m) is the normal, h_{ext} (W m⁻² K⁻¹) is the external heat transfer coefficient, ε is the thermal emissivity, and σ (W m⁻² K⁻⁴) is the Stefan-Boltzmann coefficient.

The heat transfer from the bed wall to the ambient relies on the heat transfer coefficient, which may be calculated from Nusselt number using the following correlation [44]:

$$Nu = \frac{h_{ext} D_0}{k_{air}} = \left[0.60 + 0.387 \frac{Ra^{1/6}}{\left[1 + \left(\frac{0.559}{Pr_{air}} \right)^{9/16} \right]^{8/27}} \right]^2, \quad (14)$$

where D_0 (m) is the external wall diameter, k_{air} (W m⁻¹ K⁻¹) is the thermal conductivity of the air at average temperature (of both the wall

and the ambient temperatures), Pr_{air} is the air Prandtl number, and Ra is Rayleigh number at the average temperature.

For the adiabatic walls:

$$\left(\frac{\partial T_w}{\partial n}\right)_w = 0. \quad (15)$$

2.6.2. Interfaces between walls and adsorbent

The convection heat transfer through the interface between the bed and wall is estimated from the local heat conduction Eq. (16).

$$k_{\text{eff}} \left(\frac{\partial T}{\partial n}\right)_w = h_{\text{int}}(T - T_w) = k_{\text{local}} \left(\frac{\partial T}{\partial n}\right)_{\text{local}} \quad (16)$$

Here, h_{int} ($\text{W m}^2 \text{K}^{-1}$) is the internal convection heat transfer coefficient calculated automatically by Fluent from the last term in Eq. (16). In addition,

$$\nabla y_i = 0. \quad (17)$$

2.6.3. Inlet boundary conditions

The mass and heat transfer at the bed inlet could be expressed as the diffusion quantities in balance with those corresponding to advection.

$$-\varepsilon D_{i,m} \nabla y_i = \vec{v} \cdot (y_i|_- - y_i|_+) \quad (18)$$

$$-\varepsilon k_{\text{eff}} \nabla T = \vec{v} \cdot \rho (h_i|_- - h_i|_+) \quad (19)$$

2.6.4. Outlet boundary conditions

Mass and heat fluxes at the outlet can be written as:

$$\nabla y_i = 0, \quad (20)$$

$$\nabla T = 0. \quad (21)$$

2.6.5. Centerlines (in 2D) and symmetry planes (in 3D)

The mass and heat fluxes at the axisymmetric axis and symmetry planes are:

$$\nabla y_i = 0, \quad (22)$$

$$\nabla T = 0. \quad (23)$$

2.7. Material properties

The materials used in the models were adsorbents (13X and Mg-MOF-74), gases (CO_2 and N_2), and the stainless-steel wall. Thus, the thermal properties of each species and wall material were taken as polynomial functions of temperature. The gas mixture density was

calculated using the ideal gas law, the thermal heat capacity was estimated from the mixing law, and the thermal conductivity and viscosity were evaluated from the mass-weighted-mixing law. These properties are described by the following equations.

The thermal properties of a single gas are:

$$C_{p,i} = A + BT + CT^2 + DT^3 + ET^3 \text{ (J kg}^{-1} \text{ K}^{-1}\text{)}, \quad (24)$$

$$k_i = A + BT + CT^2 + DT^3 + ET^3 \text{ (W m}^{-1} \text{ K}^{-1}\text{)}, \quad (25)$$

$$\mu_i = A + BT + CT^2 + DT^3 + ET^3 \text{ (Pas)}. \quad (26)$$

The constants of Eqs. (24)–(26) are shown in Table 1.

For stainless steel, $\rho = 7941 \text{ kg m}^{-3}$, $C_w = 358.98 + 0.487394 T - 2.65708 \times 10^{-7} T^2 \text{ J kg}^{-1} \text{ K}^{-1}$, and $k = 15.14 \text{ W m}^{-1} \text{ K}^{-1}$.

The heat capacity of the gas mixture is expressed by the mixing law.

$$C_p = \sum_i x_i C_i \quad (27)$$

Here, x_i is the molar fraction of species. Generally, the thermal inertia of the bed is

$$(\rho C_p)_{\text{bed}} = (\rho C_p)_{\text{gas}} + \rho_s (C_{p,s} + qMC_{p,g}). \quad (28)$$

The last term in Eq. (28) contains the heat capacity of the adsorbed amounts. The molecular weight, M , should be in kg mol^{-1} .

The thermal conductivity and viscosity of the gas mixture are determined by the following mass-weight-mixing laws:

$$k = \sum_i \frac{x_i k_i}{\sum_j x_j \phi_{ij}}, \quad (29)$$

$$\mu = \sum_i \frac{x_i \mu_i}{\sum_j x_j \phi_{ij}}, \quad (30)$$

$$\phi_{ij} = \frac{\left[1 + \left(\frac{\mu_i}{\mu_j}\right)^{1/2} \left(\frac{M_j}{M_i}\right)^{1/4}\right]^2}{\left[8 \left(1 + \frac{M_i}{M_j}\right)\right]^{1/2}}. \quad (31)$$

The mass dispersion coefficient suggested for the laminar low Reynolds number is given as [45]:

$$D_{\text{disp}} = 0.508 u \frac{d_p}{Re^{0.02}}. \quad (32)$$

If the Reynolds number satisfies the condition of ($Sc Re \varepsilon \geq 0.3$), the appropriate correlation of mass dispersion coefficient is given by Eq. (33) [46].

$$D_{\text{disp}} = 1.317 \frac{D_{m,g}}{\varepsilon} (\varepsilon Re Sc)^{1.392} \quad (33)$$

Table 1
Polynomial constants for gas components thermal properties.

Thermal properties	Constants of C_p equation	Constants of k equation	Constants of μ equation
CO_2	A = 491.702 B = 1.43603 C = -0.0007742 D = 0 E = 0	A = -0.00694154 B = 7.53746×10^{-5} C = 7.53746×10^{-5} D = 0 E = 0	A = -1.10128×10^{-6} B = 5.89863×10^{-8} C = -1.74847×10^{-11} D = 0 E = 0
N_2	A = 938.6992 B = 0.3017911 C = -8.109228×10^{-5} D = 8.263892×10^{-9} E = $-1.537235 \times 10^{-13}$	A = 0.004737109 B = 0.004737109 C = -1.122018×10^{-8} D = 1.454901×10^{-12} E = $-7.871726 \times 10^{-17}$	A = 7.473306×10^{-6} B = 4.083689×10^{-8} C = 4.083689×10^{-8} D = 1.305629×10^{-15} E = $-8.177936 \times 10^{-20}$
H_2O	A = 1609.791 B = 0.740494 C = -9.129035×10^{-6} D = -3.81392×10^{-8} E = 4.80227×10^{-12}	A = -0.007967996 B = 6.881332×10^{-5} C = 4.49046×10^{-8} D = $-9.099937 \times 10^{-12}$ E = 6.173314×10^{-16}	A = -4.418944×10^{-6} B = 4.687638×10^{-8} C = $-5.389431 \times 10^{-12}$ D = 3.202856×10^{-16} E = 4.919179×10^{-22}

2.8. Model validation and vacuum pressure swing adsorption cases

2.8.1. Validation

The PSA model has been validated against the experimental data reported by Dantas et al. [18] for a fixed-column bed filling with zeolite 13X. Four steps were carried out to represent a full PSA cycle, that is, pressurization (20 s), feed (100 s), blowdown (70 s), and purge (70 s). All important parameters and column properties are shown in Table 2. The purpose of the pressurization process was to raise the pressure of the bed before the feed step to about 1.3 bar by feeding in pure N₂. Then, the bed was fed by a mixed flow containing CO₂/N₂ (15% CO₂, 85% N₂ by volume) at 1.3 bar and 323 K. The CO₂ desorption was carried out by blowdown and purge processes. The bed pressure was minimized to 0.1 bar for the blowdown process using vacuum pump so that most the adsorbed CO₂ was removed from the bed. The remaining adsorbed CO₂ could be reduced by purging at about 0.187 bar and 323 K. The detailed boundary conditions are shown in Fig. 2. A complete PSA cycle (1st cycle) for both of the experimental and 1D simulation modeling [18] and the present 2D and 3D simulations are compared.

2.8.2. Vacuum pressure swing adsorption cases

A single bed was adopted to simulate five steps of PSA: pressurization, feed, rinse, blowdown, and purge. The pressurization process (20 s) was used to raise the pressure of the bed from 2 up to 130 kPa using pure N₂. Then, the feed process took place with a mixed flow containing CO₂/N₂ (15% CO₂, 85% N₂ (vol.%)) at 1.3 bar and 323 K. After a stipulated feed time (250 s), the pure CO₂ was introduced to the bed to rinse the remaining N₂ inside the bed void for about (40 s). The devoted times for feed and rinse processes were fixed in all cases to avoid the violation of the adsorption breakpoint, that is, the point at which the outlet CO₂ concentration is less than 5% of that at the inlet. The breakpoint violation leads to the loss of CO₂ to the atmosphere, which should not occur. In the blowdown process, CO₂ was desorbed from the bed by evacuating the bed to about 2 kPa. During the blowdown process, most of the captured CO₂ was removed from the bed. The remaining amount of adsorbed CO₂ could be reduced by a purge process (by applying 10 mL/min of pure N₂). The bed and system properties isotherms for VPSA cases are described in Tables 3 and 4. The blowdown and purge steps were investigated to find the optimal desorption operation time, as described in Table 5. The detailed boundary conditions of the five steps are shown in Fig. 4. The first cycle of all cases was devoted to fill the bed with CO₂ up to breakpoint by feed and rinse processes; therefore, the feed time of the first cycle was longer than that of the others. This was done to achieve the cyclic steady state earlier using fewer cycles.

Carbon dioxide and nitrogen equilibrium isotherms at different temperatures have been reported by Mason [47], as shown in Fig. 3. It is clear that Mg-MOF-74 has high a CO₂ adsorption capacity compared to that of N₂. The adsorption quantities of both gases decrease significantly on increasing the temperature. The dual-site Langmuir model was used for predicting the equilibrium adsorbed amounts of the gases at different temperatures, as suggested by Mason [47]. Table 4 shows the dual-site Langmuir parameters required for estimating the equilibrium adsorbed values for CO₂ and N₂.

2.9. VPSA performance

The most important criteria in swing adsorption processes are the CO₂ purity and recovery. The CO₂ purity is the amount of pure CO₂ (molar basis) in the produced CO₂, while the CO₂ recovery is the ratio of the amount of produced carbon dioxide to that fed to the adsorbent bed. The CO₂ purity and recovery may be calculated as formulated in Eqs. (34) and (36).

$$\text{Purity of CO}_2 = \frac{\int_{t_{\text{blowdown}}}^{t_{\text{endpurge}}} F_{\text{CO}_2} dt}{\sum_i \int_{t_{\text{blowdown}}}^{t_{\text{endpurge}}} F_i dt} \quad (34)$$

$$\text{Recovery of CO}_2 = \frac{\int_{t_{\text{blowdown}}}^{t_{\text{endpurge}}} F_{\text{CO}_2} dt}{\int_0^{t_{\text{endpurge}}} F_{\text{CO}_2} dt} \quad (35)$$

$$F_i = Q_F C_i \quad (36)$$

Here, F_i (mol s⁻¹) is the molar flow rate of component i (CO₂ and N₂). For a more useful performance analysis, the estimation of CO₂ productivity and VPSA energy consumption can be written as Eqs. (37) and (38).

$$\text{Productivity of CO}_2 = \frac{\int_{t_{\text{blowdown}}}^{t_{\text{endpurge}}} F_{\text{CO}_2} M_{\text{CO}_2} dt - \int_{t_{\text{rinse}}}^{t_{\text{endrinse}}} F_{\text{CO}_2} M_{\text{CO}_2} dt}{t_{\text{cycle}} m_s} \quad (37)$$

Here, M_{CO_2} (kg mol⁻¹) is the molecular weight of CO₂, t_{cycle} (h) is the total time of one repeated cycle, and m_s (kg) is the adsorbent mass.

The energy consumed by the vacuum pumps and blowers is [48]:

$$E_{\text{VPSA}} = \int \frac{\gamma}{\gamma-1} \frac{Q_F \epsilon_{\text{tot}} CRT}{\eta} \left[\left(\frac{P_{\text{max}}}{P_{\text{min}}} \right)^{\frac{\gamma-1}{\gamma}} - 1 \right] dt, \quad (38)$$

where η is the compressor efficiency, which was assumed to be 0.72, γ is the specific heat capacity of the gas, C (mol m⁻³) is the gas concentration, Q_F (m³ s⁻¹) is the volumetric flow rate at the bed outlet, and ϵ_{tot} is the total bed porosity ($\epsilon_{\text{tot}} = \epsilon + (1-\epsilon)\epsilon_p$). The integration is applied for every step of consumed energy and then the total energy consumed during the full cycle is the sum of the consumed energy for each step.

To calculate the CO₂ capture cost for an assumed 500-MW power plant with a specific emission of 0.83 kg CO₂ emitted by kWh of electricity generated [36], the operating capture cost (\$ tonne CO₂⁻¹) was calculated as:

$$\text{Capture cost} = \frac{\text{Power}_{(\text{CO}_2, \text{VPSA})} \times 10^6 \times \frac{\text{\$}}{\text{kWh}}}{1 - \text{em} \times \text{Power}_{(\text{CO}_2, \text{VPSA})}}, \quad (39)$$

where $\text{Power}_{(\text{CO}_2, \text{VPSA})}$ (MW h kg CO₂⁻¹) is the VPSA power consumption, em (kg CO₂ emitted by kWh produced) is the specific emission, and $\frac{\text{\$}}{\text{kWh}}$ is the electricity price which is assumed \$0.1 kWh⁻¹ [36].

3. Results and discussion

To demonstrate the reliability of the UDF-Fluent CFD, the code results have been compared to the results of experiment, and the VPSA

Table 2

Properties of the bed column and 13X used in the experimental work [18] and the present simulation.

Properties	Value
Bed Length, L	0.83 m
Bed diameter, d_{int}	0.021 m
Column wall thickness, l	0.0041 m
Column wall specific heat capacity, C_w	500 J kg ⁻¹ K ⁻¹
Column wall density	8238 kg m ⁻³
Particle density, ρ	1228.5
Bed void fraction, ϵ	0.62
Solid Specific heat, C_s	920 J kg ⁻¹ K ⁻¹
CO ₂ maximum adsorbed concentration, q_{m, CO_2}	5.09 mol kg ⁻¹
N ₂ maximum adsorbed concentration, q_{m, N_2}	3.08 mol kg ⁻¹
Toth constant, n_{CO_2}	0.429
Toth constant, n_{N_2}	0.869
Toth constant, K_{CO_2}	4.31×10^{-9} Pa ⁻¹
Toth constant, K_{N_2}	8.81×10^{-10} Pa ⁻¹
CO ₂ adsorption heat, ΔH_{CO_2}	-29380 J mol ⁻¹
N ₂ adsorption heat, ΔH_{N_2}	-17190 J mol ⁻¹

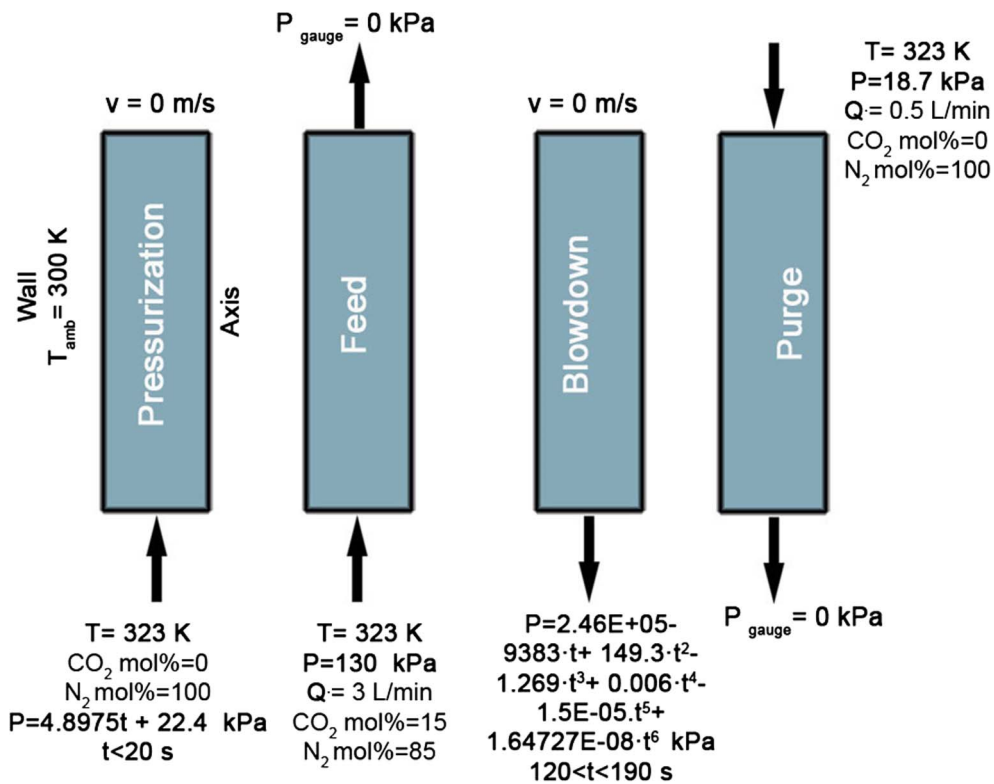


Fig. 2. Boundary conditions for the four steps of the 1st PSA cycle based on experimental data [18].

Table 3
Bed geometry and adsorption and thermal properties of the Mg-MOF-74 bed.

Properties	Value
Bed length, L	0.07 m
Bed diameter, D	0.004 m
Bed wall thickness	0.001 m
Bed density, ρ_s	297 kg m ⁻³
Adsorbent specific heat capacity, $C_{p,s}$	900 J kg ⁻¹ K ⁻¹
Adsorbent thermal conductivity, k_s	0.3 W m ⁻¹ K ⁻¹
Particle density, ρ_p	911 kg m ⁻³
Adsorbent particle size, d_p	0.0002 m
Bed porosity, ε	0.674
CO ₂ adsorption time constant coefficient, k_{L,CO_2}	0.137 s ⁻¹
N ₂ adsorption time constant coefficient, k_{L,N_2}	0.313 s ⁻¹
CO ₂ adsorption heat, ΔH_{CO_2}	-(42492.6 - 6568.83q + 3973.75 q ² - 959.838 q ³ + 69.1208 q ⁴) J mol ⁻¹ [47]
N ₂ adsorption heat, ΔH_{N_2}	-18000 J mol ⁻¹ [47]

process has been investigated using the code.

3.1. Mesh independence

The 2D adsorbent bed domain was meshed using structure quadrilateral elements. The grid independence was determined using Mg-MOF-74 at an inlet flow rate of 20 standard cubic centimeters per minute (sccm) at 300 K and 101.3 kPa for the adsorbent bed shown in

Table 4
Equilibrium isotherm parameters for Mg-MOF-74 [47].

Gas species	$q_{m,1}$ (mmol g ⁻¹)	$q_{m,2}$ (mmol g ⁻¹)	$K_{0,1}$ (Pa ⁻¹)	$K_{0,2}$ (Pa ⁻¹)	$-\Delta H_1$ (J mol ⁻¹)	$-\Delta H_2$ (J mol ⁻¹)
CO ₂	6.8	9.9	2.44×10^{-11}	1.39×10^{-10}	42,000	24,000
N ₂	14	–	4.96×10^{-10}	–	18,000	–

Table 5
Cases of VPSA regeneration (blowdown and purge) times.

Case	Blowdown Time (s)	Purge time (s)
1	150	50
2	150	100
3	150	150
4	100	100
5	200	100

Fig. 1. The thermal and adsorption properties are described in Tables 3 and 4. Fig. 5 shows CO₂/N₂ concentration breakthrough for four different number of cells (1120, 1320, 1600, and 1980 cells). All selected grids show the same concentration ratio values, indicating that the cell numbers were sufficient to present an accurate simulation. For the 3D bed, the cell size was the same as that chosen for the 2D simulation.

3.2. Model validation

PSA is an important continuous separation method, facilitating the adsorption and desorption processes by changing the applied pressure in some steps. The PSA model has been validated against experimental work [18] for one cycle. Fig. 6 shows the CO₂ molar flow rate of a complete PSA cycle (1st cycle) for both of the experimental and the 1D simulation modeling [18] and the present 2D and 3D simulation studies. The results shown in Fig. 6 confirm that the CO₂ molar flow rate of the 2D and 3D simulations have a much better agreement with those of experiment [18] in comparison with the results of 1D simulation. This can be attributed to the existence of the radial diffusion of both mass

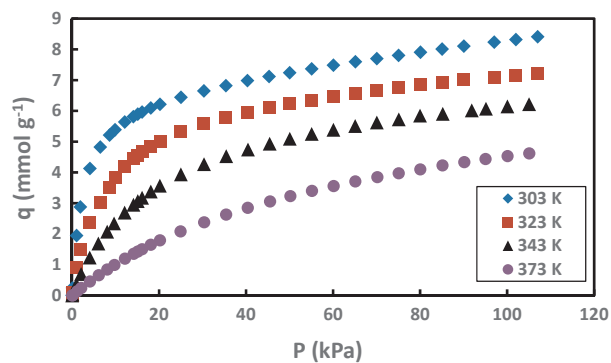
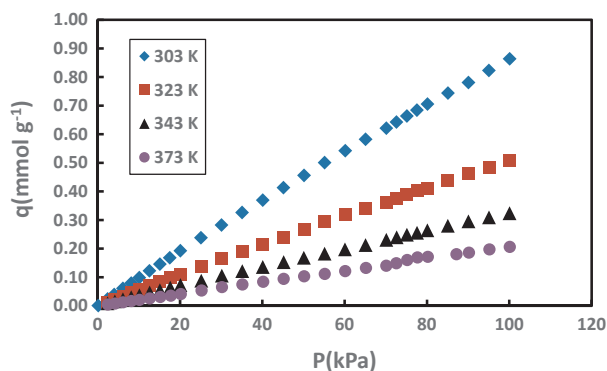
(a) CO₂ adsorption isotherms.(b) N₂ adsorption isotherms.

Fig. 3. Equilibrium adsorption isotherms at different temperatures for Mg-MOF-74: (a) CO₂ and (b) N₂ [47].

and heat transfer in the 2D and 3D models and the thermal diffusion term in the porous bed energy equation. The influence of θ -dimension on the molar flow rate values is small, so that the two-dimensional model is sufficient for cylindrical beds.

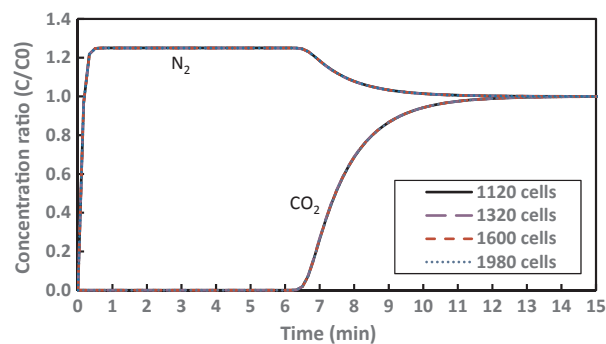


Fig. 5. Mesh independence as a comparison of CO₂/N₂ concentration ratio profiles for 1120, 1320, 1600, and 1980 cells.

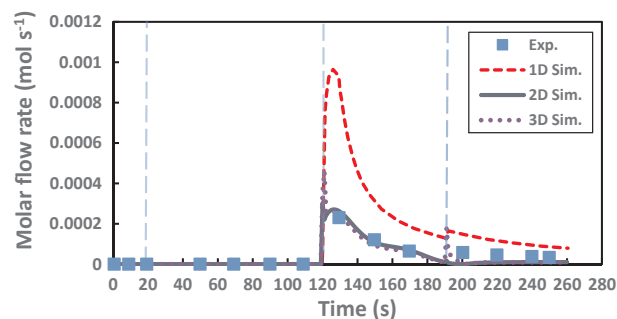


Fig. 6. A comparison of the CO₂ molar flow rate history between the experimental work, the 1D simulation [18], and the present 2D and 3D simulations over the first PSA cycle.

3.3. Comparison between 2D and 3D VPSA simulations

A comparison between the 2D and 3D VPSA simulations was made for the thermal and adsorption conditions listed in Tables 3 and 4 and shown in Fig. 4. The VPSA process included five steps: pressurization, feed, rinse, blowdown, and purge for 20, 250, 40, 100, 40 s, respectively. The CO₂ uptake during the first three cycles is shown in Fig. 7. As evident, the bed adsorbed about 7.6 mmol g⁻¹ of CO₂. However, it could only recycle about 4.5 mmol g⁻¹ under the operating pressure

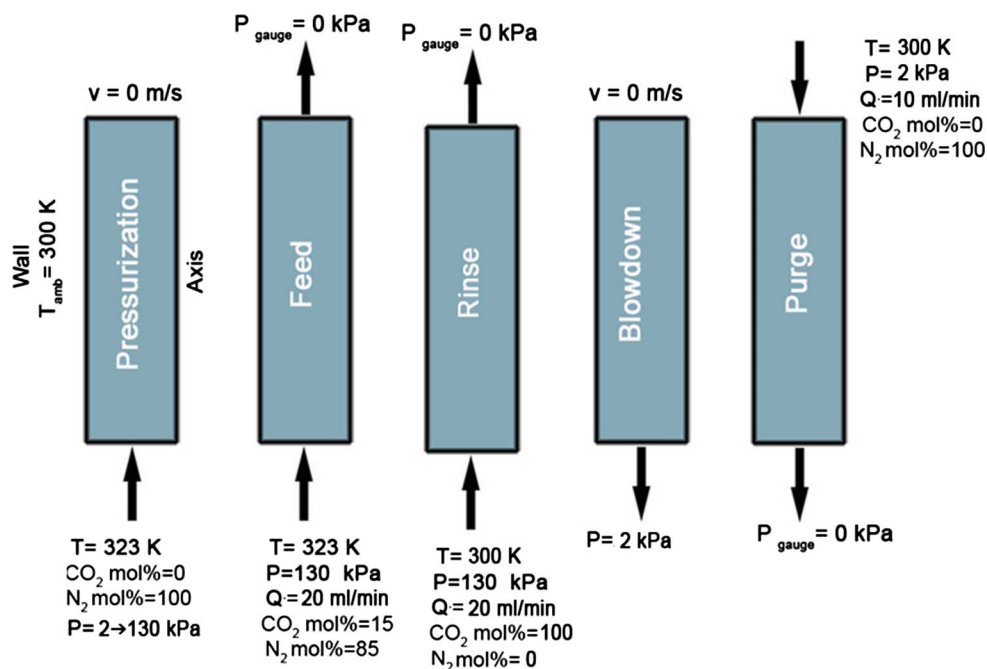


Fig. 4. Boundary conditions for the five steps in the VPSA process.

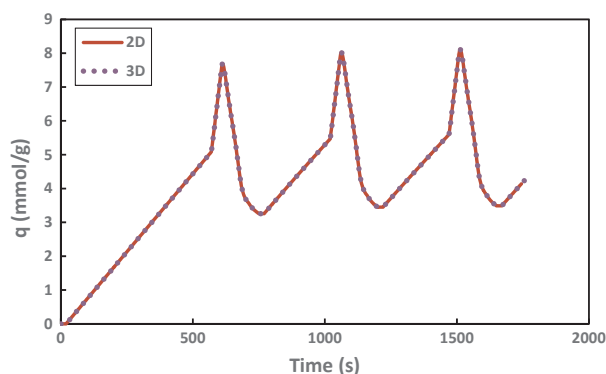


Fig. 7. A comparison of CO₂ adsorbed amounts between 2D and 3D VPSA over three cycles.

(2–130 kPa). About 3.5 mmol g⁻¹ CO₂ remained in the adsorbent bed without desorption under the pressure of the blowdown and purge steps (2 kPa). To desorb some of this quantity (3.5 mmol g⁻¹), the pressure should be less than 2 kPa or the blowdown and purge times should be extended, which would result in lower energy consumption and lower CO₂ productivity. The CO₂ uptake values for the both 2D and 3D overlap indicate that the 2D simulation is sufficient to model VPSA under the considered geometry.

Fig. 8 shows the temperature distribution along the bed for the both 2D and 3D beds at selected times (1200, 1220, 1350, 1470, 1510, 1560, 1610, and 1650 s) during all VPSA steps of a complete repeated cycle (after the seventh cycle). Obviously, the bed temperature increased by a few degrees during the pressurization process, while the temperature of the hottest zone of the bed column increased to almost 307 K during the feed step because of the CO₂ adsorption process. Then, the temperature increased to 309 K during the rinse step because of the adsorption of more CO₂ because the CO₂ entered the bed alone. Throughout the blowdown process, the temperature dropped down to almost 299 K in the final third zone and was about 297 K in the remaining zone of the column because of the huge drop in the pressure values and because of the desorption process, which consumed some energy. The temperature continually decreased during the purge process because of the desorption of some CO₂ from the bed under N₂ purging at low pressure (2 kPa). The minimum temperature recorded during the desorption process was about 296 K.

Fig. 9 shows the CO₂ mass fraction at the same selected times discussed in Fig. 8. The mass fraction at the beginning of the pressurization step was high because the start time of pressurization process occurred at the end of a previous cycle's purge step. At the end of pressurization step, the CO₂ mass fraction was about zero because of the filling of the bed with pure N₂. During the feed process, the CO₂ mass fraction (about 0.217; the corresponding molar fraction is 0.15) was moving through the bed. This parameter (CO₂ mass fraction) increased to 1 in the rinse step under a pure CO₂ feed at the bed inlet. This value (CO₂ mass fraction = 1) remained constant in the remaining steps because of the absence of N₂. The CO₂ uptake contours are shown in Fig. 10. Evidently, the CO₂ uptake throughout the bed was a minimum at 3.4 mmol g⁻¹ and increased during the feed and rinse steps consecutively because of the CO₂ feed at the bed inlet. This amount decreased in the blowdown and purge steps because of the desorption processes at low pressure (2 kPa) and the purging N₂ (during the purge step). Again, the 2D and 3D simulations gave close results to each other with negligible differences, indicating that 2D modeling is sufficient to predict such cases for the considered bed geometry. The heat and mass transfer calculations in θ -direction (angular direction) could be neglected. However, the three-dimensional simulation has the potential for the modeling of complex geometries. The presence of the three-dimensional modeling results in Figs. 8–10 is only to show the potential of the developed UDF-Fluent model to simulate 3D VPSA.

3.4. VPSA cases

The VPSA was studied for eleven cycles to show the cyclic stability for the same 2D bed shown in Figs. 1 and 4 and described in Table 3, which is composed of five steps including pressurization, feed, rinse, blowdown, and purge for about 20, 250, 40, 100, and 40 s, respectively. Fig. 11 shows the average bed pressure over eleven repeated cycles of the five steps. The pressure values fluctuate between 130 and 2 kPa during the adsorption (feed + rinse) and desorption (blowdown + purge) processes, respectively. The history of CO₂/N₂ molar flow rates is shown in Fig. 12. All in all, nitrogen appeared at the bed outlet during the feed and rinse steps, whereas CO₂ was dominant during the blowdown and purges processes because the application of a vacuum, which results in the loss of attractive forces between Mg-MOF-74 and CO₂, thereby drawing out most of the adsorbed CO₂. Clearly, the cyclic steady state started, roughly, from the third cycle. However, the fully steady state cycle started at the seventh cycle in terms of all the operating and performance parameters.

Fig. 13 shows the history of CO₂ uptake over eleven cycles. Almost 4.6 mmol g⁻¹ CO₂ was successfully recycled under the operating pressure range (130 to 2 kPa). The sharp lines during the adsorption process arise from the CO₂ uptake throughout the rinse step owing to the CO₂ adsorption at high CO₂ pressure (130 kPa) compared to those during the feed step (19.5 kPa).

To investigate the effect of the blowdown and purge times (desorption time) on the VPSA performance, five cases (Table 5) were compared in terms of CO₂ purity, recovery, and productivity, as well as the energy consumed during the process, assuming that the efficiency of the compressors and vacuum pumps is 0.72. The comparison was made when the cycles had attained steady state in each case. Fig. 14 focuses on the CO₂ purity recovery and productivity for tuning the blowdown times to between 100 and 300 s. The increase in the blowdown time improved the CO₂ recovery (from 98.45% to 98.6%) and decreased the purity (from 97.3% to 97.1%). Actually, these minor changes in the CO₂ purity and recovery are not significant, suggesting that the lowest time (100 s) might be sufficient for the blowdown process. The CO₂ productivity values also support the short blowdown period (100 s) because the time increase results in lower productivity because there is no significant desorption of CO₂ during this extended period.

The effect of the purge time on the VPSA performance is shown in Fig. 15. Clearly, increasing the purge time from 50 to 150 s increased the CO₂ recovery from 97.2% to 99.1%, respectively, but reduced both

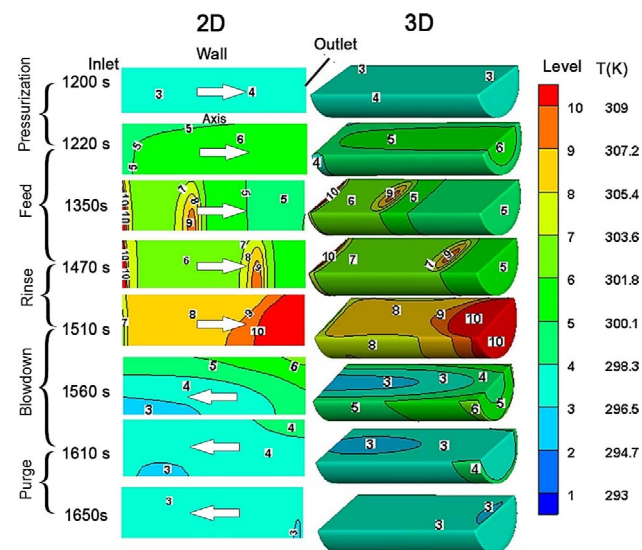


Fig. 8. A comparison of temperature contours of the bed between the 2D and 3D VPSA models during a steady state cycle.

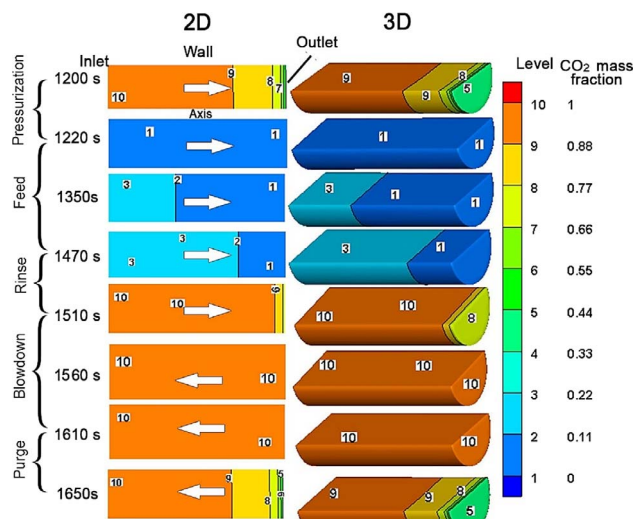


Fig. 9. A comparison of the CO₂ mass fraction between the 2D and 3D VPSA models during a steady state cycle.

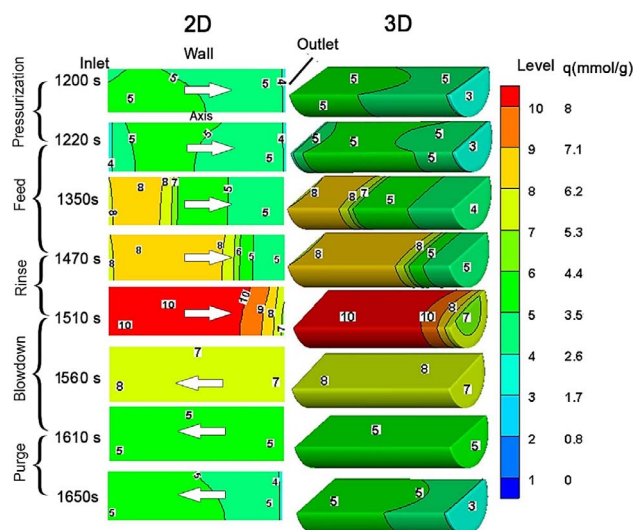


Fig. 10. A comparison of CO₂ adsorbed amounts between the 2D and 3D VPSA models during a steady state cycle.

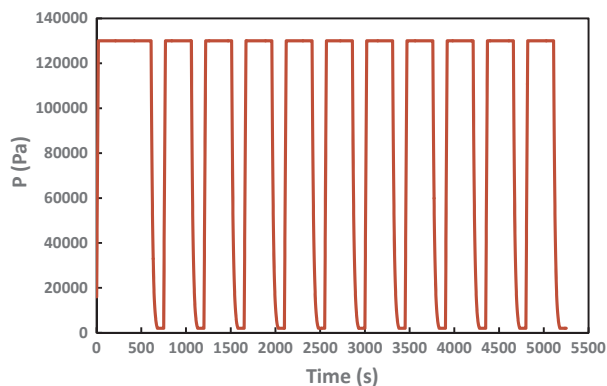


Fig. 11. Pressure history of eleven VPSA cycles (pressurization = 20 s, feed = 250 s, rinse = 40 s, blowdown = 100 s, and purge = 40 s).

the CO₂ purity (from 98.1 to 96.4) and productivity (from 0.67 to 0.58 kg CO₂ h⁻¹ kg MOF⁻¹). Therefore, the trivial increase in the CO₂ recovery values on increasing purge time was sacrificed to prioritize the

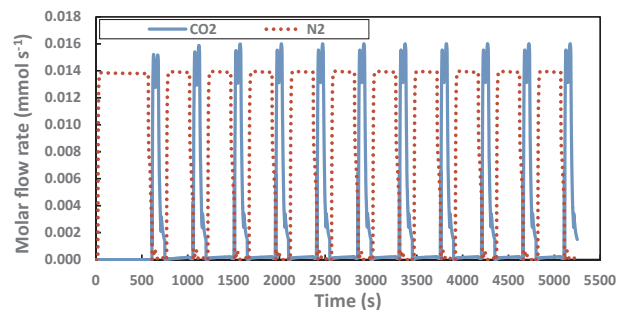


Fig. 12. CO₂/N₂ molar flow rate of eleven VPSA cycles (pressurization = 20 s, feed = 250 s, rinse = 40 s, blowdown = 100 s, and purge = 40 s).

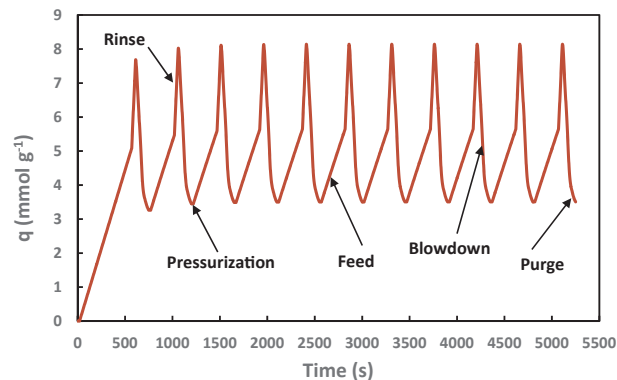


Fig. 13. CO₂ uptake over eleven VPSA cycles (pressurization = 20 s, feed = 250 s, rinse = 40 s, blowdown = 100 s, and purge = 40 s).

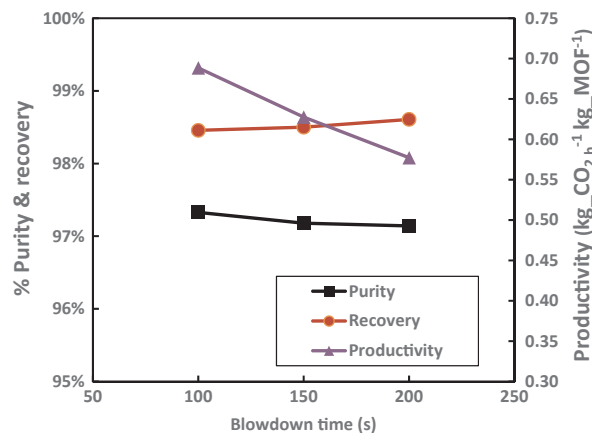


Fig. 14. Effect of blowdown time on the CO₂ purity, recovery, and productivity of the VPSA process (pressurization = 20 s, feed = 250 s, rinse = 40 s, and purge = 100 s).

CO₂ purity and productivity. The calculated power consumption of the CO₂ separation utilizing VPSA is shown in Fig. 16 for both blowdown and purging times. The power consumption required for increasing the blowdown time was almost the same (67 kWh tonne CO₂⁻¹) for all blowdown times (100, 150, and 200 s). This trend arises because the prolonged times balance out the amount of desorbed CO₂. In contrast, the increase in the purge time increased the power consumption from 64 to about 70 kWh tonne CO₂⁻¹ for the 50 and 150 s cases, respectively. Extending the purge time increased the energy consumption without desorbing substantial amounts of CO₂, as well as increasing the overall time of the VPSA cycle. However, good performance can be achieved at a blowdown time about 150 s and purge time of about 50 s. The CO₂ purity, recovery, productivity, and power consumption were estimated to be 98.1%, 97.3%, 0.67 (kg CO₂ h⁻¹ kg MOF⁻¹), and 64.2 kWh tonne CO₂⁻¹, respectively. However, selecting blowdown

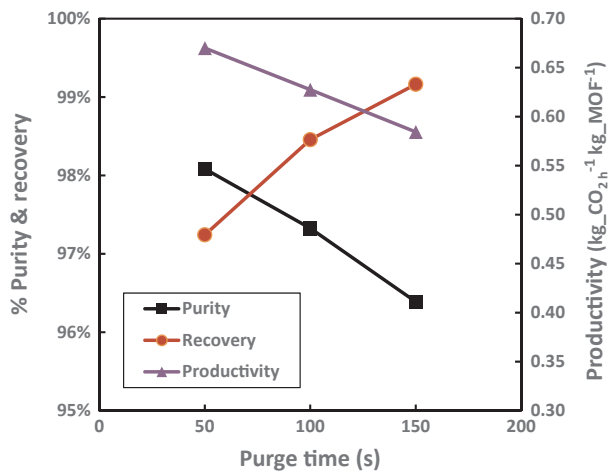


Fig. 15. Effect of purge time on the CO₂ purity, recovery, and productivity of the VPSA process (pressurization = 20 s, feed = 250 s, rinse = 40 s, and blowdown = 150 s).

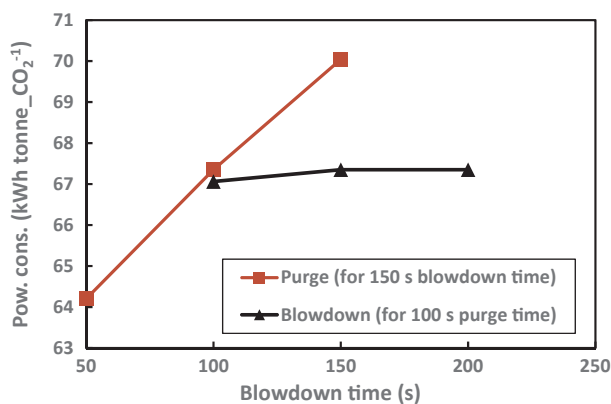


Fig. 16. Effect of blowdown and purge times on the VPSA power consumption (pressurization = 20 s, feed = 250 s, and rinse = 40 s).

and purge times of 100 and 40 s (the same cases shown in Figs. 11–13) yielded the optimal CO₂ purity, recovery, productivity, and power consumption of 98.3%, 95.7%, 0.731 kg_CO₂ h⁻¹ kg_MOF⁻¹, and 63.89 kWh tonne_CO₂⁻¹, respectively. Reducing the purge time to less than 40 s may result in a drop in the CO₂ productivity to less than 90%, which is not desirable.

Notably, the bed used in this model was very small (length = 0.07 m, inner diameter = 0.4 cm) to minimize the computational time. In contrast, actual VPSA applications require large beds. For this reason, we ran extra simulations using a longer bed (1 m) with the same (0.4 cm) and wider inner diameter (1 cm) to show the VPSA performance in such beds. Another important point is that the particle size of the adsorbent should be sufficiently large to minimize the pressure drop through the real long beds. We, therefore, selected two different adsorbent particle sizes: 1 mm for Modified-bed (1) (length = 1 m, inner diameter = 0.4 cm) and 2 mm for Modified-bed (2) (length = 1 m, inner diameter = 1 cm). The modified parameters are listed in Table 6, and the other parameters (unmodified) were kept as listed in Tables 3 and 4 and shown in Fig. 4. The times for the pressurization, feed, rinse, blowdown, and purge steps were tuned until the performance indices were optimized. The time steps were 20, 250, 35, 250, and 100 s for pressurization, feed, rinse, blowdown, and purge respectively, for both the modified beds with the exception that the rinse step was 30 s for Modified-bed (2) to avoid the release of large amounts of CO₂ into the environment at the bed outlet. The feed, rinse, and purge inlet velocity values were 0.378, 0.378, and 0.189 m s⁻¹, respectively. It is worth mentioning that the adsorption isotherms used

for Modified bed (1) and Modified bed (2) were assumed to be the same of those of 0.2 mm particle-size; whereas, in real cases, the adsorption quantities are usually decreased by adding binder materials. This assumption is made due to the absence of the isotherms data of large particle size (> 1 mm) for Mg-MOF-74 in the published literature. Also, the pelletizing processes are usually optimized in such a way the adsorption capacity of adsorbents to be as close as possible to those of virgin powders. The new VPSA performance indices for Modified-bed (1) were about 95.3%, 94.8%, 0.50 kg_CO₂ h⁻¹ kg_MOF⁻¹, and 68.71 kWh tonne_CO₂⁻¹ for the CO₂ purity, recovery, and productivity, and process power consumption, respectively; in contrast, those for Modified-bed (2) were about 94.2%, 91.0%, 0.47 kg_CO₂ h⁻¹ kg_MOF⁻¹, and 63.35 kWh tonne_CO₂⁻¹, as shown in Table 6. These performance indices for both modified beds still show a substantial improvement in CO₂ VPSA separation when using Mg-MOF-74 compared to conventional adsorbents.

The CO₂ uptake for Modified-bed (1) was higher than that of Modified-bed (2), as shown in Fig. 17. This is because of the increase of the bed temperature for the larger diameter bed. For example, the maximum temperature at the bed middle was about 327 K (during the rinse step) for the wider bed (Modified-bed (2); $D = 1$ cm) in comparison to about 308 K for the smaller diameter bed ($D = 0.4$ cm), as shown in Fig. 18. The adsorption process is exothermic, and the thermal diffusion of the adsorbents (including Mg-MOF-74) is low, resulting in the slow the heat dissipation from the bed to the surrounding environment, thus increasing the bed temperature and decreasing the CO₂ uptake. For this reason, we highly recommend using many small-diameter tubes (tube banks) as adsorbent beds for CO₂ adsorption separation in actual applications instead of using one or few large-diameter tubes; however, the economic study upon both capital and operative costs should be conducted before selecting either large-diameter tubes or tube banks. The high CO₂ purity, recovery, and productivity (95.3%, 94.8%, and 0.50 kg_CO₂ h⁻¹ kg_MOF⁻¹, respectively) of the smaller diameter bed (Modified-bed (1)) was due to the efficient cooling of the bed as a result of selecting a small bed diameter, which resulted in improved adsorption uptake of CO₂ (Table 6 and Fig. 17). However, the energy consumption of Modified-bed (2) (228.1 kJ kg_CO₂⁻¹) is lower than that of Modified-bed (1) (247.34 kJ kg_CO₂⁻¹, see Table 6) because the pressure drop of Modified-bed (2) is small in comparison to that of Modified-bed (1) (Fig. 18). The low-pressure drop of Modified-bed (2) was a result of the larger adsorbent particle size (2 mm). The maximum pressure drop was obtained in the blowdown step (Fig. 18), especially when the bed pressure reached its lowest level (about 2 kPa) because of the increasing amount of CO₂

Table 6

Bed geometry, LDF parameters, and VPSA performance indices of the modified Mg-MOF-74 beds.

Bed and LDF parameters		Performance indices	
<i>Modified-bed (1)</i>			
Bed length, L	1 m	CO ₂ purity	95.3%
Adsorbent particle size, d_p	0.001 m	CO ₂ recovery	94.8%
Bed diameter, D	0.004 m	CO ₂ productivity, kg_CO ₂ h ⁻¹ kg_MOF ⁻¹	0.50
CO ₂ adsorption time constant coefficient, k_{L,CO_2}	0.1215 s ⁻¹	Energy consumption, kJ kg_CO ₂ ⁻¹	247.34
N ₂ adsorption time constant coefficient, k_{L,N_2}	0.2889 s ⁻¹	Power consumption, MW h tonne_CO ₂ ⁻¹	68.71
<i>Modified-bed (2)</i>			
Bed length, L	1 m	CO ₂ purity	94.2%
Adsorbent particle size, d_p	0.002 m	CO ₂ recovery	91.0%
Bed diameter, D	0.01 m	CO ₂ productivity, kg_CO ₂ h ⁻¹ kg_MOF ⁻¹	0.47
CO ₂ adsorption time constant coefficient, k_{L,CO_2}	0.1163 s ⁻¹	Energy consumption, kJ kg_CO ₂ ⁻¹	228.1
N ₂ adsorption time constant coefficient, k_{L,N_2}	0.2351 s ⁻¹	Power consumption, MW h tonne_CO ₂ ⁻¹	63.35

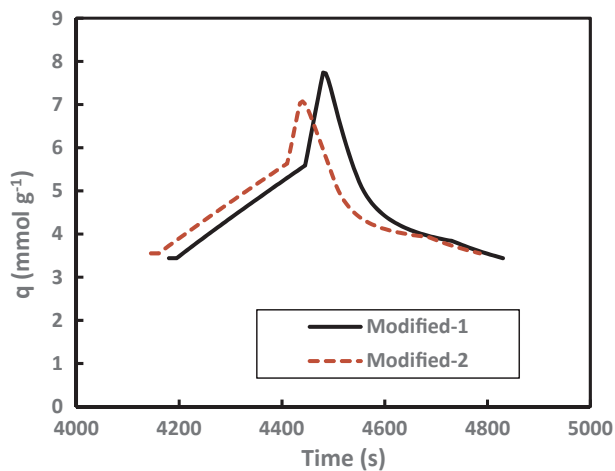


Fig. 17. CO₂ uptake history of Modified-bed (1) ($L = 1$ m, $D = 0.4$ cm, and $dp = 1$ mm) and Modified-bed (2) ($L = 1$ m, $D = 1$ cm, and $dp = 2$ mm) during the seventh cycle (cyclic steady state).

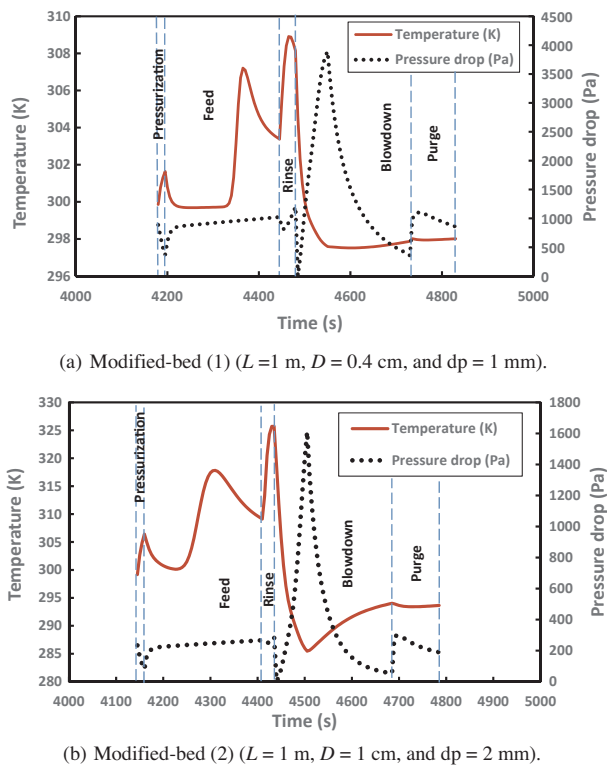


Fig. 18. Temperature profile at the bed middle and pressure drop history between the bed inlet and outlet for (a) Modified-bed (1) and (b) Modified-bed (2) during the seventh cycle (cyclic steady state).

(velocity) leaving the bed. As the velocity increased, the pressure drop for the same adsorbent particle size and bed porosity increased.

If we assume these modified VPSA beds (as a part of tube banks of adsorbent beds) are used to separate CO₂ in a 500-MW power plant [36], the operating CO₂ capture cost would be \$6.87 and \$6.34 tonne_{CO₂}⁻¹ for Modified-bed (1) and Modified-bed (2), respectively, while the lowest operating cost reported in literature was \$12 tonne_{CO₂}⁻¹ using the VSA method and 13X as adsorbent [36]. These operating cost values (\$6.3 and \$6.7 per tonne of CO₂ captured) have not been bettered, demonstrating another advantage of using Mg-MOF-74 for CO₂ separation processes in real power plants and the industrial sector.

Table 7 shows a comparison of the CO₂ separation performance of the present VPSA process and some swing adsorption processes reported in the literature. The present VPSA process improves the CO₂ adsorption separation for two main reasons: the utilization of Mg-MOF-74 as adsorbent, which adsorbs/desorbs significant quantities of CO₂, and the optimization of the regeneration (desorption) time. The advantage of Mg-MOF-74 is its high affinity for CO₂.

4. Conclusion

The VPSA process for separating CO₂ from CO₂/N₂ mixtures using Mg-MOF-74 was investigated numerically. A CFD model was developed using a user defined function (written in C) connected to the ANSYS Fluent program to model the adsorption and kinetic models and adjust the source terms of the mass, momentum, and energy equations. The developed model was employed to carry out two- and three-dimensional simulations. The model has been validated against published pressure swing adsorption experimental data. The multidimensional modeling has shown that the 2D model is sufficiently accurate to represent the CO₂ separation process by VPSA for the chosen geometry. The VPSA process was composed of five steps (pressurization, feed, rinse, blowdown, and purge) with an operating pressure range between 2 and 130 kPa and inlet feed temperature of 323 K. The blowdown and purge periods were studied to explore the optimum VPSA performance for the bed length of 0.07 m and the adsorbent particle size 0.0002 m. The optimal CO₂ purity and recovery were about 98.3% and 95.7%, respectively. In addition, the corresponding CO₂ productivity and process power consumption were evaluated to be 0.731 kg_{CO₂} h⁻¹ kg_{MOF}⁻¹ and 63.89 kW h tonne_{CO₂}⁻¹ (with estimated cost of \$6.39 tonne_{CO₂}⁻¹), respectively. However, the longer bed (1 m) and larger adsorbent particle size (0.001 m) had VPSA performance indices of about 95.3%, 94.8%, 0.50 kg_{CO₂} h⁻¹ kg_{MOF}⁻¹, and 68.71 kW h tonne_{CO₂}⁻¹ for the CO₂ purity, recovery, and productivity, and process power consumption, respectively. The corresponding estimated cost was about \$6.87 tonne_{CO₂}⁻¹, revealing a substantial improvement in the carbon dioxide adsorption separation in a comparison to those of published works. We found that increasing the adsorbent particle size decreased the process power consumption, whereas increasing the bed diameter decreased the VPSA performance.

Acknowledgements

We thank and acknowledge support from King Abdulaziz City for

Table 7
A comparison of CO₂ separation performances amongst different materials and processes.

Adsorbent	Process	CO ₂ (vol.%)	Purity (%)	Recovery (%)	Productivity (kg _{CO₂} h ⁻¹ kg _{Adsorbent} ⁻¹)	Energy consumption (kJ kg _{CO₂} ⁻¹)	Study	Refs.
13X-APG	VPSA	15.5–16.5	95.6	73–82.3	0.0387	1790–2140	Exp.	[25]
AC	VPSA	15	95.3	74.4	0.035	723.6	Sim.	[31]
13X	PSA	10.5	99	80	–	2300–2800	Exp.	[16]
5A	TSA	10	> 94	75–85	0.052	6120–6460	Exp.	[49]
5A	PTSA	10	95.2	94.8	0.069	3800	Sim.	[50]
Mg-MOF-74	VPSA	15	95.3	94.8	0.50	247.34	Sim.	This work

Science and Technology (KACST), the Carbon Capture and Sequestration Technology Innovation Center (CCS-TIC #32-753) under Project CCS10, and the Deanship of Scientific Research at KFUPM, Dhahran, Saudi Arabia.

References

- [1] Lee S-Y, Park S-J. A review on solid adsorbents for carbon dioxide capture. *J Ind Eng Chem* 2015;23:1–11.
- [2] Guardian. antarctic-ship-stranding-delights-climate-change-sceptics; 2014. Available from: < www.theguardian.com > .
- [3] D'Alessandro DM, McDonald T. Toward carbon dioxide capture using nanoporous materials. *Pure Appl. Chem.* 2010;83(1).
- [4] IPCC. Special Report on Carbon Dioxide Capture and Storage, Metz ODEB, Coninct H, Loos M, Meyer L, Editor; 2005.
- [5] Ben-Mansour R, Habib MA, Bamidele OE, Basha M, Qasem NAA, Peedikakkal A, et al. Carbon capture by physical adsorption: materials, experimental investigations and numerical modeling and simulations – a review. *Appl Energy* 2016;161:225–55.
- [6] Songolzadeh M, Ravanchi MT, Soleimani M. Carbon dioxide capture and storage: a general review on adsorbents. *World Acad Sci Eng Technol* 2012;70:225–32.
- [7] Choi S, Drese JH, Jones CW. Adsorbent materials for carbon dioxide capture from large anthropogenic point sources. *ChemSusChem* 2009;2(9):796–854.
- [8] Siriwardane RV, Shen M-S, Fisher EP, Poston JA. Adsorption of CO₂ on molecular sieves and activated carbon. *Energy Fuels* 2001;15(2):279–84.
- [9] Mazumder S, van Hemert P, Busch A, Wolf KHAA, Tejera-Cuesta P. Flue gas and pure CO₂ sorption properties of coal: a comparative study. *Int J Coal Geol* 2006;67(4):267–79.
- [10] Plaza MG, González AS, Pevida C, Pis JJ, Rubiera F. Valorisation of spent coffee grounds as CO₂ adsorbents for postcombustion capture applications. *Appl Energy* 2012;99:272–9.
- [11] Li J-R, Sculley J, Zhou H-C. Metal-organic frameworks for separations. *Chem Rev* 2012;112(2):869–932.
- [12] Adhikari AK, Lin K-S. Improving CO₂ adsorption capacities and CO₂/N₂ separation efficiencies of MOF-74(Ni, Co) by doping palladium-containing activated carbon. *Chem Eng J* 2016;284:1348–60.
- [13] Yang D-A, Cho H-Y, Kim J, Yang S-T, Ahn W-S. CO₂ capture and conversion using Mg-MOF-74 prepared by a sonochemical method. *Energy Environ Sci* 2012;5(4):6465–73.
- [14] Cavenati S, Grande CA, Rodrigues AE. Separation of mixtures by layered pressure swing adsorption for upgrade of natural gas. *Chem Eng Sci* 2006;61(12):3893–906.
- [15] Chaffee AL, Knowles GP, Liang Z, Zhang J, Xiao P, Webley PA. CO₂ capture by adsorption: materials and process development. *Int J Greenhouse Gas Control* 2007;1(1):11–8.
- [16] Cho SH, Park JH, Beum HT, Han SS, Kim JN. A 2-stage PSA process for the recovery of CO₂ from flue gas and its power consumption. *Stud. Surf. Sci. Catal.* 2004;153:405–10.
- [17] Choi WK, Kwon TI, Yeo YK, Lee H, Song HK. Optimal operation of the pressure swing adsorption (PSA) process for CO₂ recovery. *Korean J. Chem. Eng.* 2003;20:617–23.
- [18] Dantas TLP, Luna FMT, Silva LJ, Torres AEB, de Azevedo DCS, Rodrigues AE, et al. Carbon dioxide–nitrogen separation through pressure swing adsorption. *Chem Eng J* 2011;172(2–3):698–704.
- [19] Gomes VG, Yee KWK. Pressure swing adsorption for carbon dioxide sequestration from exhaust gases. *Sep Purif Technol* 2002;28(2):161–71.
- [20] Krishnamurthy SVR, Rao S, Guntuka P, Sharratt R, Haghpahan A, Rajendran M, et al. CO₂ capture from dry flue gas by vacuum swing adsorption: a pilot plant study. *AIChE J* 2014;60(5):1830–42.
- [21] Harlick PJE, Sayari A. Applications of pore-expanded mesoporous silicas. 3. triamine silane grafting for enhanced CO₂ adsorption. *Ind Eng Chem Res* 2006;45(9):3248–55.
- [22] Maurin G, Llewellyn PL, Bell RG. Adsorption mechanism of carbon dioxide in faujasites: grand canonical monte carlo simulations and microcalorimetry measurements. *J Phys Chem B* 2005;109(33):16084–91.
- [23] Akhtar F, Andersson L, Keshavarzi N, Bergström L. Colloidal processing and CO₂ capture performance of sacrificially templated zeolite monoliths. *Appl Energy* 2012;97:289–96.
- [24] Cheung O, Bacsik Z, Liu Q, Mace A, Hedin N. Adsorption kinetics for CO₂ on highly selective zeolites NaKA and nano-NaKA. *Appl Energy* 2013;112:1326–36.
- [25] Wang L, Yang Y, Shen W, Kong X, Li P, Yu J, et al. Experimental evaluation of adsorption technology for CO₂ capture from flue gas in an existing coal-fired power plant. *Chem Eng Sci* 2013;101:615–9.
- [26] Wang L, Liu Z, Li P, Yu J, Rodrigues AE. Experimental and modeling investigation on post-combustion carbon dioxide capture using zeolite 13X-APG by hybrid VTSA process. *Chem Eng J* 2012;197:151–61.
- [27] Wang M, Yao L, Wang J, Zhang Z, Qiao W, Long D, et al. Adsorption and regeneration study of polyethylenimine-impregnated millimeter-sized mesoporous carbon spheres for post-combustion CO₂ capture. *Appl Energy* 2016;168:282–90.
- [28] McGurk SJ, Martín CF, Brandani S, Sweatman MB, Fan X. Microwave swing regeneration of aqueous monoethanolamine for post-combustion CO₂ capture. *Appl Energy* 2017;192:126–33.
- [29] Su F, Lu C, Chung A-J, Liao C-H. CO₂ capture with amine-loaded carbon nanotubes via a dual-column temperature/vacuum swing adsorption. *Appl Energy* 2014;113:706–12.
- [30] Zhu X, Shi Y, Cai N. Integrated gasification combined cycle with carbon dioxide capture by elevated temperature pressure swing adsorption. *Appl Energy* 2016;176:196–208.
- [31] Shen C, Liu Z, Li P, Yu J. Two-stage VPSA process for CO₂ capture from flue gas using activated carbon beads. *Ind Eng Chem Res* 2012;51(13):5011–21.
- [32] Raganati F, Ammendola P, Chirone R. On improving the CO₂ recovery efficiency of a conventional TSA process in a sound assisted fluidized bed by separating heating and purging. *Sep Purif Technol* 2016;167:24–31.
- [33] Plaza MG, González AS, Pevida C, Rubiera F. Green coffee based CO₂ adsorbent with high performance in postcombustion conditions. *Fuel* 2015;140:633–48.
- [34] Ridha FN, Manovic V, Macchi A, Anthony EJ. CO₂ capture at ambient temperature in a fixed bed with CaO-based sorbents. *Appl Energy* 2015;140:297–303.
- [35] Zhao B, Liu F, Cui Z, Liu C, Yue H, Tang S, Liu Y, Lu H, Liang B. Enhancing the energetic efficiency of MDEA/PZ-based CO₂ capture technology for a 650 MW power plant: Process improvement. *Appl Energy* 2017;185(Part 1):362–75.
- [36] Zhang J, Webley PA, Xiao P. Effect of process parameters on power requirements of vacuum swing adsorption technology for CO₂ capture from flue gas. *Energy Convers Manage* 2008;49(2):346–56.
- [37] Westendorf TC, Joel Chen, Wei Farnum, Rachael Perry, Robert Spiry, Irina Wilson, et al. Bench-Scale Process for Low-Cost Carbon Dioxide (CO₂) Capture Using a Phase-Changing Absorbent; 2015. Available from: < <https://www.osti.gov/scitech/biblio/1182556> > .
- [38] Dantas TLP, Luna FMT, Jr IJS, Torres AEB, Azevedo DCSd, Rodrigues AE, et al. Carbon dioxide–nitrogen separation through pressure swing adsorption. *Chem Eng J* 2011;172:698–704.
- [39] Da Silva FA, Silva JA, Rodrigues AE. A General package for the simulation of cyclic adsorption processes. *Adsorption* 1999;5(3):229–44.
- [40] Ansys-Fluent; 2016. Available from: < <http://www.ansys.com> > .
- [41] Dantas TLP, Luna FMT, Silva LJ, de Azevedo DCS, Grande CA, Rodrigues AE, et al. Carbon dioxide–nitrogen separation through adsorption on activated carbon in a fixed bed. *Chem Eng J* 2011;169(1–3):11–9.
- [42] He W, Lv W, Dickerson JH. Gas Diffusion Mechanisms and Models, in *Gas Transport in Solid Oxide Fuel Cells*; 2014. Cham: Springer International Publishing. p. 9–17.
- [43] Shafeeyan MS, Wan Daud WMA, Shamiri A. A review of mathematical modeling of fixed-bed columns for carbon dioxide adsorption. *Chem Eng Res Des* 2014;92(5):961–88.
- [44] Incropera, Frank PD, David P. Fundamentals of heat and mass transfer 2007. J. Wiley.
- [45] Dantas TLP, Luna FMT, Silva Jr LJ, Torres AEB, de Azevedo DCS, Rodrigues AE, et al. Modeling of the fixed - bed adsorption of carbon dioxide and a carbon dioxide - nitrogen mixture on zeolite 13X. *Braz J Chem Eng* 2011;28(3):533–44.
- [46] Funazukuri T, Kong C, Kagei S. Effective axial dispersion coefficients in packed beds under supercritical conditions. *J. Supercrit. Fluids* 1998;13(1–3):169–75.
- [47] Mason JA, Sumida K, Herm ZR, Krishna R, Long JR. Evaluating metal–organic frameworks for post-combustion carbon dioxide capture via temperature swing adsorption. *Energy Environ Sci* 2011;4(8):3030.
- [48] Susarla N, Haghpahan R, Karimi IA, Farooq S, Rajendran A, Tan LSC, et al. Energy and cost estimates for capturing CO₂ from a dry flue gas using pressure/vacuum swing adsorption. *Chem Eng Res Des* 2015;102:354–67.
- [49] Merel J, Clausse M, Meunier F. Experimental investigation on CO₂ post-combustion capture by indirect thermal swing adsorption using 13X and 5A zeolites. *Ind Eng Chem Res* 2008;47(1):209–15.
- [50] Mendes PAP, Ribeiro AM, Gleichmann K, Ferreira AFP, Rodrigues AE. Separation of CO₂/N₂ on binderless 5A zeolite. *J CO₂ Utiliz* 2017:224–33.